YALE JOURNAL OF BIOLOGY AND MEDICINE 85 (2012), pp.217-228.

FOCUS: BIOMEDICAL ENGINEERING

Toward Large-Scale Computational Fluid-Solid-Growth Models of Intracranial Aneurysms

Paolo Di Achille and Jay D. Humphrey*

Department of Biomedical Engineering, Yale University, New Haven, Connecticut

Complementary advances in medical imaging, vascular biology, genetics, biomechanics, and computational methods promise to enable the development of mathematical models of the enlargement and possible rupture of intracranial aneurysms that can help inform clinical decisions. Nevertheless, this ultimate goal is extremely challenging given the many diverse and complex factors that control the natural history of these lesions. As it should be expected, therefore, predictive models continue to develop in stages, with new advances incorporated as data and computational methods permit. In this paper, we submit that large-scale, patient-specific, fluid-solid interaction models of the entire circle of Willis and included intracranial aneurysm are both computationally tractable and necessary as a critical step toward fluid-solid-growth (FSG†) models that can address the evolution of a lesion while incorporating information on the genetically and mechanobiologically determined microstructure of the wall.

INTRODUCTION

Intracranial aneurysms are focal dilatations of the arterial wall that occur in and near the circle of Willis, the primary network of arteries that supply blood to the brain. These lesions occur in approximately 2 percent to 4 percent of the general population and, despite advances in neurosurgery and neuroradiology, continue to be responsible for significant morbidity and mortality [1,2]. There is a need for an increased understanding of all three aspects of the natural history of these lesions (i.e., genesis, enlargement, and rupture) and, in particular, how risk factors such as age, genetics, sex, and hemodynamics contribute to lesion de-

*To whom all correspondence should be addressed: Jay D. Humphrey, PhD, Department of Biomedical Engineering, Yale University, 55 Prospect St., New Haven, CT 06520; Tele: 203-432-6428; Email: jay.humphrey@yale.edu.

†Abbreviations: CT, computed tomography; WSS, wall shear stress; FSG, fluid-solid-growth; RCR, resistance, compliance, resistance.

Keywords: saccular aneurysm, hemodynamics, image-based model, wall deformation

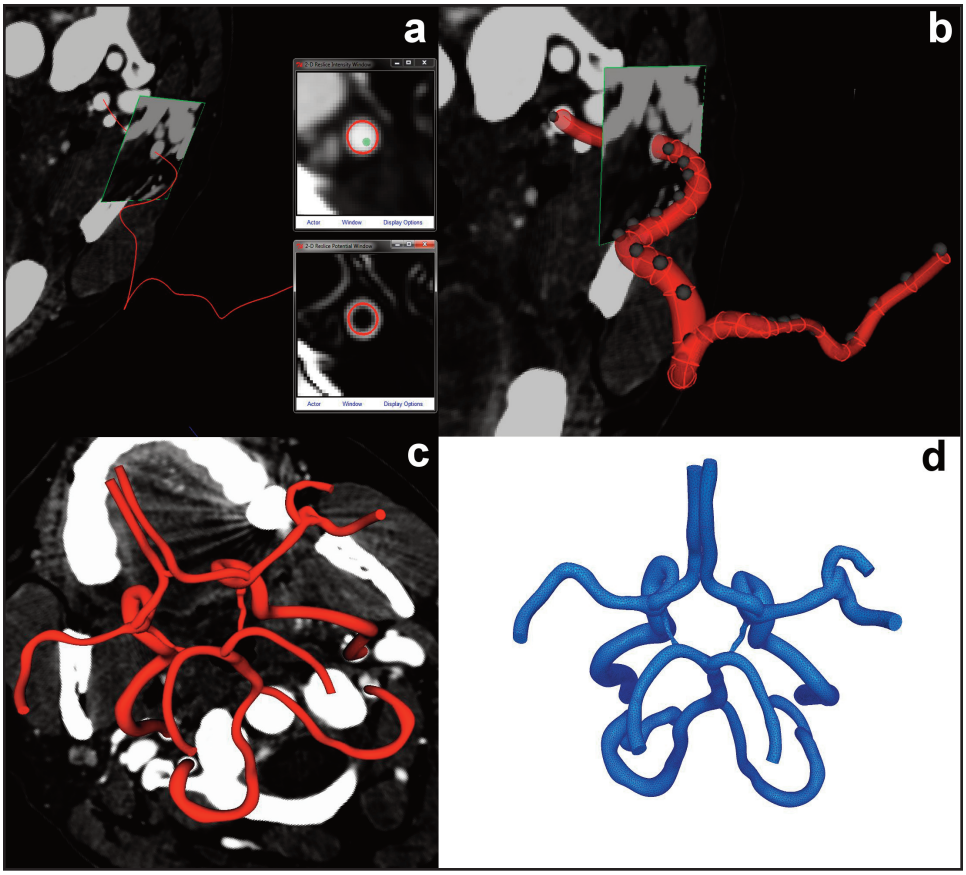

Figure 1. Procedure for building a patient-specific geometric model of the circle of Willis from diagnostic CT-angiography. a) Image segmentation of the luminal boundary at one cross-section of a cerebral artery. **b)** Construction of a solid model passing through several segmented boundaries, noted by the grey spheres. **c)** Final geometric model after joining the major arteries together and appropriately smoothing the model at junctions and bifurcations. **d)** Finite element computational model constructed using ~500,000 tetrahedral elements, which was found to be necessary to solve the fluid-solid-interaction problem numerically.

velopment [3,4]. Computational models can help elucidate complex interactions among diverse factors and consequently are increasingly used to complement experimentally and clinically measurable information.

It is intuitive that intracranial aneurysms rupture when mechanical stresses in the vascular wall exceed the intrinsic strength of the wall. These stresses depend on three key factors: the geometry and material properties of the lesion and the applied loads. Although a need remains for increased spatial resolution to quantify wall thickness, advances in medical imaging enable one to quantify the overall geometry of the cerebral arterial circulation and included aneurysms on a patient-specific basis. The material properties (e.g., stiffness) of the aneurysmal wall result from the composition, organization, and interactions of intramural constituents, which can vary regionally and evolve as the lesion enlarges; they are much more difficult to quantify and depend on the genetics, mechanobiological responses to hemodynamic loading, and medical history. The primary loads that act on an intracranial aneurysm are the hemodynamically induced tractions on the luminal surface (i.e., blood pressure and wall shear stresses resulting from blood flow) and the perivascular trac-

tions that result from the lesion interacting mechanically with its surroundings. Catheter-based measurements can provide information on intraluminal pressures, but such measurements are neither routine nor useful in inferring wall shear stresses. Fortunately, advances in imaging (e.g., phase-contrast MRI or Doppler ultrasound) can provide some information on flows within major arteries as well as the aneurysms, which in turn can help in estimating both pressures and wall shear stresses, provided that one employs an appropriate "fluid-solid-interaction" model. Indeed, an advantage of fluid-solid-interaction models is that they can be used to perform parametric studies over a range of flow conditions, wall properties and thicknesses, and perivascular tractions that can help estimate ranges of possible wall stresses and thus rupture potential.

In this paper, we submit further that computational models of fluid-solid interactions within large portions of the cerebral vasculature are both tractable and essential for informing complementary models of the growth and remodeling processes that depend on the aforementioned risk factors and promise to provide predictive capability. As illustrative examples, we provide two patient-specific geometric models of the circle of Willis and associated saccular aneurysm and use the open source code SimVascular to compute spatiotemporal changes in hemodynamics and wall deformations based on appropriate inlet and outlet conditions and first order approximations of wall stiffness. We conclude by discussing additional advances that will be needed to develop full fluid-solid-growth models.

METHODS

Patients and Model Construction

Computational fluid-solid-interaction models were built for two patients, each affected by a single saccular aneurysm. Briefly, geometric information was obtained from routine de-identified CT-angiograms that provided information on the entire circle of Willis as well as the lesion of interest. Patient A harbored an ~5 mm diameter aneurysm at the bifurcation between the right internal carotid and middle cerebral arteries, and Patient B harbored an ~4.5 mm diameter aneurysm at the first bifurcation of the right middle cerebral artery. The geometric models were built using a semi-automatic procedure available in the open source code SimVascular [5]. First, we used stacked image sets to approximate centerlines of the major arteries along their path through the brain (Figure 1a). We then extracted sequential 2D images of cross-sections of each artery by cutting slices orthogonal to the centerlines and approximating the luminal boundary from each image using level-set segmentation algorithms in SimVascular [6]. In this way, each vessel was assigned a set of segmented boundaries, which was then used to build a solid curve that reproduced the geometry of the lumen (Figure 1b). A final model of the entire circle of Willis was then obtained by joining the reproduced arteries and smoothing critical regions such as junctions and bifurcations (Figure 1c). For subsequent use in the finite element model, the geometric domains were subdivided into meshes of tetrahedral elements (i.e., small computational domains) with a nominal edge size of 0.6 mm (Figure 1d). The total numbers of elements for the two patient-specific geometric models were 487,107 (Patient A) and 479,574 (Patient B).

Boundary Conditions

The circle of Willis is supplied by four main arteries — the two internal carotid arteries and the two vertebral arteries — which thus served as "inlet vessels" in the model. Conversely, six primary arteries — the distal paired anterior, posterior, and middle cerebral arteries — served as "outlet vessels," for they represented terminal surfaces beyond which the downstream vasculature was not segmented. Prescribing appropriate boundary conditions at both the inlets and outlets of a model is critical for achieving accurate simulations [7,8]. Due to the lack of patient-specific measurements of far-field inflows, we employed previously reported flow waveforms at each inlet. Specifically, we

Table 1. Boundary Conditions used in the numerical simulations.

	Inlet BCs			Outlet BCs		
	Artery	*Area (cm^2)*	*Mean Flow (cm^3/s)*	*Artery*	*$R_1 + R_2$ (mmHg s ml^{-1})*	*C ml/mmHg*
Patient A	L ICA	0.146	1.41	ACAs	*80.5*	*4.7*
	R ICA	0.149	1.45			
	L VA	0.140	1.29			
	R VA	0.120	0.97	MCAs	*75.2*	*2.8*
Patient B	L ICA	0.200	2.49	PCAs	*80.5*	*5.8*
	R ICA	0.201	2.49			
	L VA	0.140	1.29			
	R VA	0.102	0.70			

ICA is internal carotid artery, VA is vertebral artery, ACA is anterior cerebral artery, MCA is middle cerebral artery, and PCA is posterior cerebral artery.

used mean, normalized flow waveforms for the internal carotid and vertebral arteries collected under physiologic conditions via a series of 17 phase contrast magnetic resonance imaging studies [9]. To scale these waveforms according to the patient-specific dimensions of the inlet arteries within our two models, we employed a modified Murray's law [10], namely

$$Q = kA^n$$

where Q is the time averaged volumetric flow rate during a cardiac cycle, A is the cross sectional area of the inlet vessel (in cm^2), and $k = 48.21$ and $n = 1.84$ are best-fit coefficients reported in [10]. Vessel areas were prescribed by computing the average of the luminal areas of three cross-sections located in close proximity to the inlet surface. In all simulations, we assumed a heartbeat rate of 60 bpm and prescribed a Womersley velocity profile at the inlet [11] that yielded the scaled flow rate; a Womersley profile reflects effects of pulsatility.

Outlet boundary conditions should capture effects that the downstream vasculature has on the region of interest, even if not modeled explicitly due to the lack of image resolution for the smaller arteries and microcirculation. With this goal in mind, a particularly appealing approach is to couple a 3D model of the hemodynamics within large vessels with a 1D lumped parameter model of the smaller vessels [7]. Among the many models proposed, the Windkessel model has found wide acceptance, for it can simulate the resistance (R) and the compliance (C) of small arteries and arterioles and the resistance (R) of the capillaries as an electrical analog. Imposing such a condition at a terminal surface is straightforward in SimVascular once the characteristic parameters are known, hence Windkessel boundary conditions were prescribed at all outlets. Specific values for the RCR parameters were extracted from a 1D model of the entire human vasculature by Reymond et al. [12]. These values, along with the prescribed inlet flows, are listed in Table 1.

Wall Properties

Intracranial arteries tend to be stiffer than their extracranial counterparts [13] and experience relatively small, although non-negligible, deformations during the cardiac cycle. Moreover, despite the stress-strain behavior being nonlinear, one can appropriately linearize this behavior over a cardiac cycle [14] and thereby use a standard stiffness modulus in a fluid-solid-interaction simulation. SimVascular currently allows only a uniform isotropic linearized behavior of a constant thickness wall, hence we prescribed a material stiffness of 588 kPa, which corresponds to the incremental modulus at 100 mmHg reported in [15], and a uniform wall thickness of 0.36 mm [16]. It is, of course,

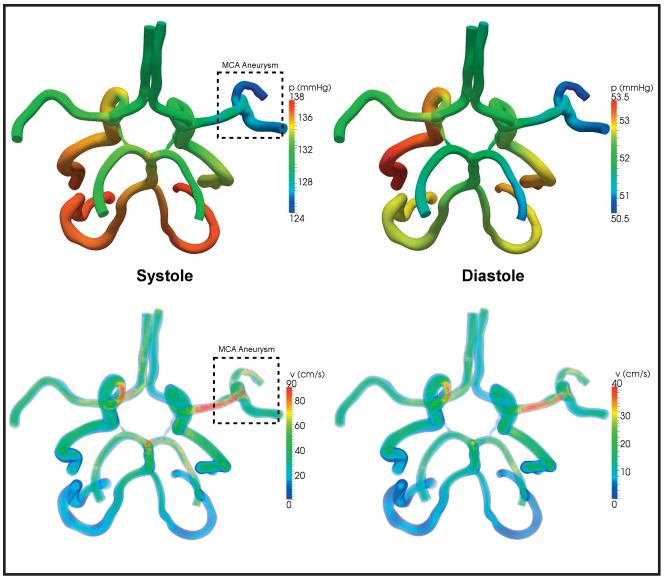

Figure 2. Overall geometric model of the circle of Willis for Patient B, with associated color-coded distributions of computed luminal pressure (top) and velocity (bottom) fields at both end systole (left) and end diastole (right). The aneurysm is located at the first bifurcation of the right middle cerebral artery (MCA). Despite the nearly symmetric inlet vessels (internal carotids and vertebrals), note the asymmetry in the computed hemodynamics due to some asymmetry in outlet vessels.

the structural stiffness (i.e., combined effects of material stiffness and wall thickness) that affects the hemodynamics.

Numerical Simulations

The 3D pulsatile fluid-solid-interaction problem was solved using a stabilized finite element method in SimVascular [17,18]. For each patient-specific geometric model and scaled inlet conditions, we conducted both a rigid wall analysis (for comparison) and a deformable wall analysis. In all cases, blood was considered as a Newtonian fluid (i.e., one with linear stress — shear rate behavior) with a viscosity of 4 cP and a density of 1.06 g/cm^3 (and thus incompressible). Preliminary studies conducted on idealized geometries revealed that initial conditions on wall displacements could be critical both in ensuring the convergence of the simulation and in minimizing the effects of transients in the deformable wall analysis, hence we conducted three preparatory simulations before every deformable wall analysis to ensure acceptable initial wall displacements. First, we conducted a steady flow analysis on a complementary rigid model to obtain the static pressure distribution; this result helped to estimate plausible distributions for the mean pressure, which were applied as initial luminal surface loads in a subsequent deformable wall analysis. Second, we prescribed the resulting displacement fields as boundary conditions in a steady flow study within the deformable model; this simulation provided the desired initial conditions for the pulsatile case in the deformable wall model.

Simulations were typically run for three cardiac cycles, but only the results of the third cycle were considered when analyzing the data. No significant differences were noticed in the fluid dynamics between the second and the third cycles, however. The time resolution for rigid wall analyses was ~0.5 ms, whereas a cardiac cycle was subdivided into 10,000 time steps (for 0.1 ms of resolution) in the deformable wall analyses. Simulations were run in parallel on the four cores of an Intel W365 processor installed on a Dell T3500 Workstation with 12 GB of RAM.

RESULTS

Recall that our primary goal herein was to build fluid-solid-interaction models that can eventually inform our growth and remodeling models and to show that such models are tractable for the entire circle of Willis, which minimizes effects of uncertainties in inlet and outlet boundary conditions. Figure 2 shows the full geometric model for Patient B, with the aneurysm visible in the vicinity of the first bifurcation of the right middle cerebral artery. The four input vessels ap-

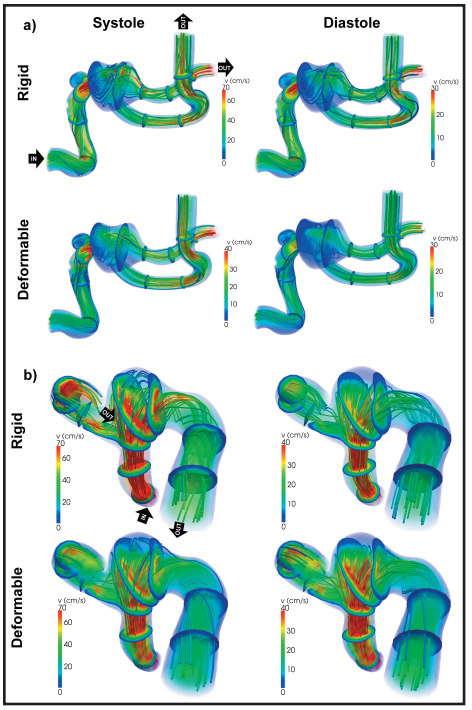

Figure 3. Comparison of fluid streamlines in the vicinity of and within the lesion for Patient A (a) and Patient B (b) based both on rigid wall and deformable wall simulations, shown at end systole (left) and end diastole (right). Among other findings, the extent of maximum velocities in the deformable model was less than that in the rigid model. Note that color scale-bars were defined over reduced (not absolute minimum-to-maximum) ranges to highlight key features of the flow fields; minimal and maximal values were thus assigned colors corresponding to the smallest and largest values on the reduced scale.

peared nearly symmetric overall, but this was not the case for the six outlet arteries — the two middle cerebral arteries appeared to have different lengths and curvatures. Shown, too, are full field results for the deformable wall simulation, specifically, the computed pressure and velocities fields at both end systole and end diastole, which were asymmetric as expected, given asymmetries in the outlet arteries. Knowing the variations in the pressure field is particularly important for building growth and remodeling models since smooth muscle cells and fibroblasts alter their gene expression in response to pressure-induced intramural stresses or strains.

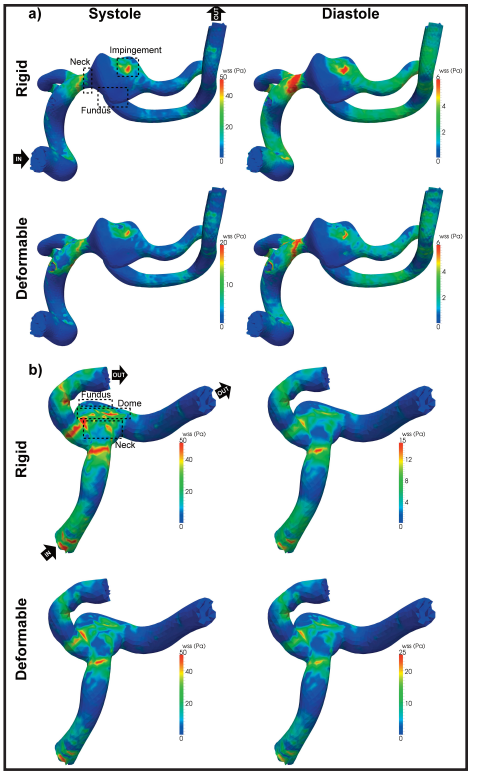

Figure 4. Similar to Figure 3 except for instantaneous wall shear stress (WSS) fields. In Patient A (a), the WSS was higher within the impingement region, where the flow impacted the vessel wall. In contrast, the fundus of the aneurysm was characterized by low WSS throughout the cardiac cycle. In Patient B (b), the lesion experienced a more uniform WSS distribution. Most of the dome of the aneurysm experienced higher WSS, while lower WSS acted on the neck as well as at the fundus. For both patients, rigid wall simulations predicted higher WSS at end systole, while the effect was reversed at end diastole. Note: Color scale-bars were defined over reduced (not absolute minimum-to-maximum) ranges to highlight key features of the flow fields; minimal and maximal values were thus assigned colors corresponding to the smallest and largest values on the reduced scale.

The hemodynamics within an aneurysm is better appreciated by focusing on results in and near the lesion. Figure 3 shows screenshots of streamlines (i.e., lines everywhere tangent to the local velocity field) at both end systole and end diastole for both patients and both the rigid wall and the deformable wall simulations. As

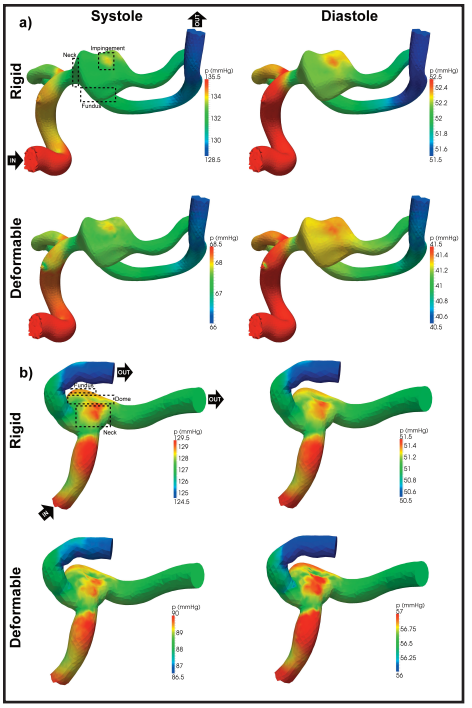

Figure 5. Similar to Figures 3 and 4, except for instantaneous pressure fields. In the lesion of Patient A (a), higher pressures were predicted within the impingement region rather than at the neck or fundus. For Patient B (b), the pressure was higher at the neck and fundus, but slightly smaller over most of the dome. Note: Color scalebars were defined over reduced (not absolute minimum-to-maximum) ranges to highlight key features of the flow fields; minimal and maximal values were thus assigned colors corresponding to the smallest and largest values on the reduced scale.

it can be seen, a relatively high-flow velocity was found in the parent arteries feeding the lesions; the largest velocity was 100 cm/s (Patient A, rigid wall model). More importantly, the aneurysmal flow in Patient A (Figure 3a) was characterized by two main vortices (or swirling flows) generated by the flow breaking down on the wall opposite the input vessel. After impacting the wall of the aneurysm, the flow velocity was attenuated by the vortices but then increased as it coalesced and entered the daughter arteries. Notice the differences in velocity magnitudes between the rigid and deformable wall simulations, however. In general, the average velocity at the core of the lesion was predicted to be higher at end systole if the wall was assumed to be rigid. In contrast, differences between the core velocities were less pronounced at end diastole for the rigid and deformable models. The aneurysmal flow in Patient B (Figure 3b) appeared to be more regular. The parent and two daughter vessels of the lesion formed a T-shape, a configuration typical of many saccular aneurysms. Consequently, the blood flow followed the lesion wall on the upper side until it reached the fundus, at which point it started back, forming a vortex and then splitting between the daughter arteries. Intraaneurysmal velocities averaged over a cardiac cycle were ~30 cm/s in the rigid wall model and ~35 cm/s in the deformable wall model, but the peak velocities were again larger for the rigid wall models (80 versus 60 cm/s).

Wall Shear Stress (WSS) is a measure of the friction that a flowing viscous fluid exerts on the wall of a blood vessel. WSS is a well-known mechano-stimulus for endothelial gene expression, and several studies have suggested that WSS is important in both the pathogenesis and enlargement of intracranial aneurysms. Investigating spatiotemporal distributions of WSS is thus of critical importance. Figure 4 shows computed WSS distributions at end systole and end diastole in and near the lesions for both patients. Including the deformability of the wall tended to reduce the magnitude of the WSS, particularly at end systole. This effect was more pronounced in Patient A. As seen in the scaled column for systole in Figure 4a, the deformable wall analysis yielded a maximum WSS of 21 Pa, whereas the rigid wall analysis predicted a three-fold higher WSS of 64 Pa in the same region. Differences between the rigid and deformable wall models were less evident at end diastole, however, where the effect seemed to be reversed. For example, within the zone of flow impingement, the WSS was 7 Pa for the rigid wall model and 10 Pa for the deformable wall model. Apart from this region of high WSS, where the flow coming from the parent artery broke down into two vortices, the lesion of Patient A was generally characterized by large regions of low WSS (2 to 3 Pa). The fundus of the aneurysm farthest from inlet

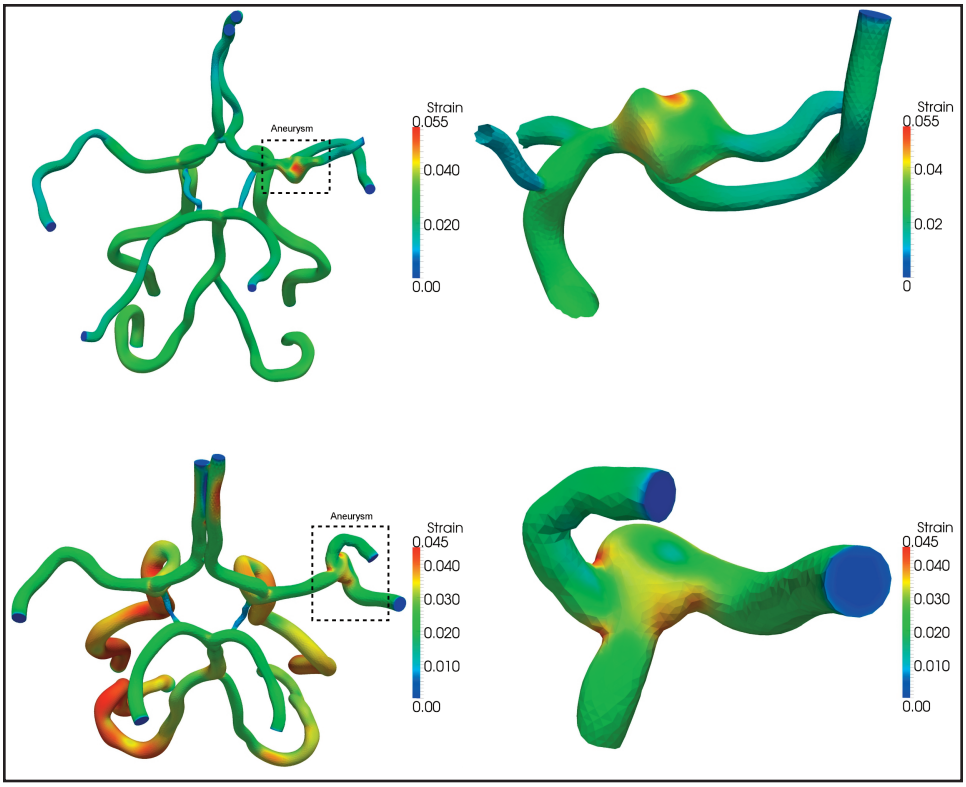

Figure 6. Color-coded distribution of computed wall strain in terms of the first invariant of the Green strain tensor. Top row: Patient A. Bottom row: Patient B. The right column shows the aneurysms in more detail. Note: Maximum values on the order of 5 percent, with the scale bar showing the full range of values from minimum to maximum.

flow had a WSS less than 0.5 Pa in the rigid wall analysis and 1 Pa in the deformable wall analysis. Results for Patient B (Figure 4b) were consistent with that which would be expected of a simpler saccular shape of the aneurysm. This lesion did not present a concentrated zone of high WSS, likely because its flow did not impact directly on the wall, as was the case for Patient A. Large regions within the dome of the lesion experienced values of WSS at end systole within the range 25 to 30 Pa for the rigid wall analysis and 15 to 20 Pa for the deformable wall analysis; again, the fundus was characterized by a smaller WSS at end diastole. Finally, the rigid wall analyses tended to under-predict the WSS in zones of flow recirculation. Overall, however, both types of analysis predicted a maximum WSS in the parent artery of the saccular aneurysm.

Conditions imposed on the stiffness of the wall proved fundamental in calculating the pressure fields throughout the circle of Willis. For both patients, the rigid wall analyses predicted a systolic/diastolic pressure range of about 135/55 mmHg at the inlet vessels. The pressure drop that drove the flow ($P_{inlet} - P_{outlet}$) was ~7 to 8 mmHg at systole and 2 to 3 mmHg at diastole, much of which (~30 percent) occurred near the site of the lesion and toward one of the daughter vessels. Figure 5 reveals slight inhomogeneities overall in the pressure fields. For both patients, the pressure was smaller at the very last segment of the parent artery, before the neck of the aneurysm. In Patient A, pressure seemed to be higher in the impingement region than in the rest of the aneurysm where the field was almost uniformly distributed. In Patient B, there was a slightly larger pressure on the frontal neck and fundus of the aneurysm. On the back of the bleb, no differences could be noticed between the neck and the dome of the aneurysm.

Finally, Figure 6 shows calculated distributions of a scalar metric of the strain (first invariant of the Green strain tensor, which is properly insensitive to rigid body motions) relative to the diastolic configuration. In Patient A, the maximum value of strain (~0.055) was predicted at the impingement region of the aneurysm, whereas vessels of the proximal circulation experienced strains of about 0.03. In Patient B, the strain distribution was overall more uniform, although the left internal carotid and vertebral arteries deformed slightly more than the corresponding vessels of the right circulation (~0.04 vs. ~0.03). On the aneurysm, the maximum strain (~0.045) was predicted at the bifurcations with the daughter vessels, while the dome and the fundus of the lesion underwent smaller deformations (~0.025).

DISCUSSION

Much remains to be learned with regard to the natural history of intracranial aneurysms, yet it is widely accepted that biomechanical factors play many different important roles [19-22]. In addition to rupture occurring when wall stress exceeds wall strength, it is now known that all primary cells of the vascular wall — endothelial, smooth muscle, fibroblasts, and even invading macrophages — are extremely sensitive to changes in their mechanical environment [23-25]. In particular, endothelial cells change their gene expression and hence production of diverse vasoactive, mitogenic, proteolytic, and inflammatory molecules in response to local changes in WSS [26,27]. Similarly, vascular smooth muscle cells and fibroblasts change their gene expression and production of myriad bioregulatory molecules in response to changes in local wall stress or strain [28,29], which, of course, result primarily from the effects of blood pressure acting on a distensible wall.

Whether motivated by the importance of WSS on endothelial biology or the relative ease of calculating wall shear versus intramural stress, most prior studies of the hemodynamics in intracranial aneurysms focused on computing WSS alone. Moreover, although it was shown many years ago that computed values of WSS are generally higher in rigid wall models, consistent with findings herein at end systole, the majority of these prior studies employed rigid wall models [30-32]. Many insightful findings have nonetheless come from such studies, including observations that regions of aneurysmal growth often correlate with regions of very low WSS and that multiple metrics of hemodynamics (e.g., the degree of concentration of WSS) correlate well with regions of rupture.

Aneurysmal enlargement and rupture clearly depend on the mechanical behavior of the vascular wall, however, and there is also a need to compute the pressure fields that distend the wall. Fortunately, advances in fluid-solid-interaction modeling now enable both wall shear and intramural stress to be computed simultaneously e.g., [33,34]. Like many of the prior rigid wall models, however, these recent fluid-solid-interaction studies of intracranial aneurysms tend to focus on only small regions of the vasculature near the aneurysm. As recently pointed out, the presence of shorter inlet lengths to the aneurysm can exacerbate uncertainties in the inlet flow boundary conditions and render it difficult to prescribe appropriate outlet conditions that affect the pressure fields, including propagation of pressure waves, that are fundamental to studying the wall mechanics [7,8,35].

In this paper, therefore, we used the open source code SimVascular, which employs a computationally efficient coupled momentum method [17] to solve fluid-solid interactions over large portions of the vasculature at reasonable computational cost (the present simulations involving ~500,000 elements were performed on a desktop computer within 5 days). That is, the equations of motion for the wall were solved together with the fluid problem without needing a dedicated mesh for the solid domain. Moreover, appropriate Windkessel boundary conditions [7] allowed realistic pressure fields to be computed throughout the entire circle of Willis and lesion. As pointed out by Humphrey and Taylor [21], however, even fluid-solid-interaction solutions alone are not

sufficient. Understanding the enlargement and rupture-risk of intracranial aneurysms requires that we also include information on the aforementioned mechanobiological responses by the cells to the computed hemodynamic loads. That is, we must account for the cell-mediated turnover of extracellular matrix that necessarily underlies the changes in lesion geometry, composition, and properties that dictate whether the lesion will continue to enlarge or rupture.

Figueroa et al. [36] outlined a possible theoretical framework to accomplish these so-called fluid-solid-growth (FSG) models, and Watton et al. [37] and Sheidaei et al. [38] have shown that such models can be implemented to study intracranial and aortic aneurysms, respectively. Briefly, because of the very different time-scales between hemodynamic changes over a cardiac cycle and growth and remodeling processes over weeks to months, FSG modeling can be accomplished via a loose coupling of fluid-solid-interaction models (as presented herein) and growth and remodeling models. The latter allow one to capture mechanobiological responses by cells that lead to a refashioning of the extracellular matrix, and hence stiffness and strength of the wall, which in turn depends in large part on the underlying genetics [39,40], as well as the hemodynamics. Given the growing importance of genetics in aneurysm research [1] and the availability of genome-wide association studies of intracranial aneurysms [41], such FSG models promise to contribute to our increasing integration of knowledge of the genetics, vascular biology, and biomechanics and thereby to yield increased insight.

In summary, the present modeling approach extends prior work by demonstrating that computationally tractable fluid-solid-interaction solutions can be achieved on image-based, patient-specific geometric models of the entire circle of Willis, which minimizes the effects of uncertainties in inlet and outlet boundary conditions on the overall solution while allowing one to prescribe conditions that are also known better. Although SimVascular proved very useful in this regard, there is yet a need to include regional variations in both wall thickness and wall properties. There is similarly a need for improved imaging to enable measurement of both regional wall thickness and distensibility, the latter both to inform and validate the model. Coupling such technical advances with theoretical advances in modeling the mechanical consequences of mechanobiological responses by cells to changing hemodynamic loads will then allow the FSG models that are needed to improve our ability to understand and predict the natural history of intracranial aneurysms and hopefully their possible response to specific interventions.

Acknowledgments: We thank Drs. M. Gunel and R. Hebert, Yale School of Medicine, for supplying the de-identified medical images; Dr. S. Sankaran, University of California — San Diego, for assistance with installing and using the code SimVascular; and Professor C.A. Figueroa, King's College London, for technical guidance. P. Di Achille was supported by a Yale University Fellowship.

REFERENCES

1. Ruigrok YM, Rinkel GJ, Wijmenga C. Genetics of intracranial aneurysms. Lancet Neurol. 2005;4(3):179-89.
2. Zacharia BE, Hickman ZL, Grobelny BT, DeRosa P, Kotchetkov I, Ducruet AF, et al. Epidemiology of Aneurysmal Subarachnoid Hemorrhage. Neurosurg Clin N Am. 2010;21(2):221-33.
3. de Rooij NK, Linn FHH, van der Plas JA, Algra A, Rinkel GJE. Incidence of subarachnoid haemorrhage: a systematic review with emphasis on region, age, gender and time trends. J Neurol Neurosurg Psychiatry. 2007;78(12):1365-72.
4. Nixon AM, Gunel M, Sumpio BE. The critical role of hemodynamics in the development of cerebral vascular disease. J Neurosurg. 2010;112(6):1240-53.
5. Schmidt JP, Delp SL, Sherman MA, Taylor CA, Pande VS, Altman RB. The Simbios National Center: systems biology in motion. Proc IEEE Inst Electr Electron Eng. 2008;96(8):1266-80.
6. Wang KC, Dutton RW, Taylor CA. Improving geometric model construction for blood flow modeling. IEEE Eng Med Biol Mag. 1999;18(6):33-9.
7. Vignon-Clementel IE, Figueroa CA, Jansen KE, Taylor CA. Outflow boundary conditions for three-dimensional finite element modeling of blood flow and pressure in arteries. Computer Methods in Applied Mechanics and Engineering. 2006;195(29-32):3776-96.

8. Anor T, Grinberg L, Baek H, Madsen JR, Jayaraman MV, Karniadakis GE. Modeling of blood flow in arterial trees. Wiley Interdiscip Rev Syst Biol Med. 2010;2(5):612-23.
9. Ford MD, Alperin N, Lee SH, Holdsworth DW, Steinman DA. Characterization of volumetric flow rate waveforms in the normal internal carotid and vertebral arteries. Physiol Meas. 2005;26:477-88.
10. Cebral JR, Castro MA, Putman CM, Alperin N. Flow-area relationship in internal carotid and vertebral arteries. Physiol Meas. 2008;29:585-94.
11. Womersley JR. Method for the calculation of velocity, rate of flow and viscous drag in arteries when the pressure gradient is known. J Physiol. 1955;127(3):553-63.
12. Reymond P, Merenda F, Perren F, Rüfenacht D, Stergiopulos N. Validation of a one-dimensional model of the systemic arterial tree. Am J Physiol Heart Circ Physiol. 2009;297(1):H208-22.
13. Wagner HP, Humphrey JD. Differential Passive and Active Biaxial Mechanical Behaviors of Muscular and Elastic Arteries: Basilar Versus Common Carotid. J Biomech Eng. 2011;133(5):051009-10.
14. Baek S, Gleason R, Rajagopal K, Humphrey J. Theory of small on large: Potential utility in computations of fluid-solid interactions in arteries. Computer Methods in Applied Mechanics and Engineering. 2007;196(31-32):3070-8.
15. Nagasawa S, Handa H, Okamura A, Naruo Y, Moritake K, Hayashi K. Mechanical properties of human cerebral arteries. Part 1: Effects of age and vascular smooth muscle activation. Surg Neurol. 1979;12(4):297.
16. Alastruey J, Parker KH, Peiró J, Byrd SM, Sherwin SJ. Modelling the circle of Willis to assess the effects of anatomical variations and occlusions on cerebral flows. J Biomech. 2007;40(8):1794-805.
17. Figueroa CA, Vignon-Clementel IE, Jansen KE, Hughes TJR, Taylor CA. A coupled momentum method for modeling blood flow in three-dimensional deformable arteries. Computer Methods in Applied Mechanics and Engineering. 2006;195(41-43):5685-706.
18. Whiting CH, Jansen KE. A stabilized finite element method for the incompressible Navier-Stokes equations using a hierarchical basis. International Journal for Numerical Methods in Fluids. 2001;35(1):93-116.
19. Humphrey JD, Canham PB. Structure, Mechanical Properties, and Mechanics of Intracranial Saccular Aneurysms. Journal of Elasticity. 2000;61(1-3):49-81.
20. Lasheras JC. The biomechanics of arterial aneurysms. Annu Rev Fluid Mech. 2007;39:293-319.
21. Humphrey JD, Taylor CA. Intracranial and Abdominal Aortic Aneurysms: Similarities, Differences, and Need for a New Class of Computational Models. Annu Rev Biomed Eng. 2008;10(1):221-46.
22. Socci L, Pennati G, Gastaldi D, Vena P. Modeling and mechanobiology of cerebral aneurysms. J Appl Biomater Biomech. 2008;6(2):63-71.
23. Lehoux S, Castier Y, Tedgui A. Molecular mechanisms of the vascular responses to haemodynamic forces. J Intern Med. 2006;259(4):381-92.
24. Dajnowiec D, Langille BL. Arterial adaptations to chronic changes in haemodynamic function: coupling vasomotor tone to structural remodelling. Clin Sci (Lond). 2007;113(1):15-23.
25. Humphrey JD. Vascular Adaptation and Mechanical Homeostasis at Tissue, Cellular, and Sub-cellular Levels. Cell Biochem Biophys. 2007;50(2):53-78.
26. Davies PF. Hemodynamic shear stress and the endothelium in cardiovascular pathophysiology. Nat Clin Pract Cardiovasc Med. 2009;6(1):16-26.
27. Chiu JJ, Chien S. Effects of disturbed flow on vascular endothelium: pathophysiological basis and clinical perspectives. Physiol Rev. 2011;91(1):327-87.
28. Li C, Xu Q. Mechanical stress-initiated signal transduction in vascular smooth muscle cells in vitro and in vivo. Cell Signal. 2007;19(5):881-91.
29. Chiquet M, Gelman L, Lutz R, Maier S. From mechanotransduction to extracellular matrix gene expression in fibroblasts. Biochim Biophys Acta. 2009;1793(5):911-20.
30. Boussel L, Rayz V, McCulloch C, Martin A, Acevedo-Bolton G, Lawton M, et al. Aneurysm Growth Occurs at Region of Low Wall Shear Stress. Stroke. 2008;39(11):2997-3002.
31. Cebral JR, Mut F, Weir J, Putman C. Quantitative Characterization of the Hemodynamic Environment in Ruptured and Unruptured Brain Aneurysms. AJNR Am J Neuroradiol. 2011;32(1):145-51.
32. Sugiyama SI, Meng H, Funamoto K, Inoue T, Fujimura M, Nakayama T, et al. Hemodynamic Analysis of Growing Intracranial Aneurysms Arising from a Posterior Inferior Cerebellar Artery. World Neurosurg. 2011 Nov 1. [Epub ahead of print.]
33. Torii R, Oshima M, Kobayashi T, Takagi K, Tezduyar TE. Fluid-structure interaction modeling of blood flow and cerebral aneurysm: Significance of artery and aneurysm shapes. Computer Methods in Applied Mechanics and Engineering. 2009;198(45-46):3613-21.
34. Bazilevs Y, Hsu M-C, Zhang Y, Wang W, Kvamsdal T, Hentschel S, et al. Computational vascular fluid–structure interaction: methodology and application to cerebral aneurysms. Biomech Model Mechanobiol. 2010;9(4):481-98.
35. Taylor CA, Figueroa CA. Patient-Specific Modeling of Cardiovascular Mechanics. Annu Rev Biomed Eng. 2009;11(1):109-34.
36. Alberto Figueroa C, Baek S, Taylor CA, Humphrey JD. A computational framework for fluid-solid-growth modeling in cardiovascular

simulations. Computer Methods in Applied Mechanics and Engineering. 2009;198(45-46):3583-602.
37. Watton PN, Selimovic A, Raberger NB, Huang P, Holzapfel GA, Ventikos Y. Modelling evolution and the evolving mechanical environment of saccular cerebral aneurysms. Biomech Model Mechanobiol. 2010;10(1):109-32.
38. Sheidaei A, Hunley SC, Zeinali-Davarani S, Raguin LG, Baek S. Simulation of abdominal aortic aneurysm growth with updating hemodynamic loads using a realistic geometry. Med Eng Phys. 2011;33(1):80-8.
39. Yasmin, O'Shaughnessy KM. Genetics of arterial structure and function: towards new biomarkers for aortic stiffness? Clin Sci (Lond). 2008;114(11):661-77.
40. Lacolley P, Challande P, Osborne-Pellegrin M, Regnault V. Genetics and pathophysiology of arterial stiffness. Cardiovasc Res. 2009;81(4):637-48.
41. Yasuno K, Bilguvar K, Bijlenga P, Low SK, Krischek B, Auburger G, et al. Genome-wide association study of intracranial aneurysm identifies three new risk loci. Nat Genet. 2010;42(5):420-5.